ADVANCED FUNCTIONAL MATERIALS
www.afm-journal.de

High-Sensitivity Flexible Thermocouple Sensor Arrays Via Printing and Photonic Curing

Md Mofasser Mallick, Leonard Franke, Andres Georg Rösch, Mohamed Hussein, Zhongmin Long, Yolita M. Eggeler, and Uli Lemmer**

Despite remarkable advances, high-performance thermoelectric (TE) materials-based thermocouples (TCs) lack mechanical robustness and flexibility. Hence, conventional low Seebeck coefficient metals (Ni, Cu, Fe) wire-junction-based TCs are used for temperature sensor applications. However, not only the sensitivity of the metal-based TC sensor is low, but also it is very difficult to fabricate a pixelated sensor using the conventional approach. In this study, high-performance $(SbBi)_2(TeSe)_3$-based printed flexible TE materials are employed to fabricate two types of shape-conformable TC-based temperature sensor arrays with 25 pixels (TSA I and TSA II). $Bi_{0.5}Sb_{1.5}Te_3$-based p-type (p-BST) printed TE film and copper are used to fabricate TSA I, and the p-type film together with the $Bi_2Te_{2.7}Se_{0.3}$-based n-type (n-BT) film is used to fabricate TSA II. A high average sensitivity (S_{exp}) value of ≈124 µV °C^{-1} for TSA I and ≈319 µV °C^{-1} for TSA II is attained with high linearity.

1. Introduction

The research on thermoelectrics, so far, has been mainly for energy harvesting,[1] waste heat recovery,[2] and cooling applications.[3,4] The TE technology is also widely employed for temperature sensor applications due to the following advantages: no resistance-related error, fast response, point temperature sensing, and wide temperature range operation.[5] For a long time, metal-based TC governed by the TE effect have been used as temperature sensors.[6] However, less effort has been put forward to enhance their sensitivities or to modify their functionalities due to the limitations in the fabrication process. A voltage is developed at an end when another junction of a TC is heated up. The produced voltage (V_{out}) is directly proportional to the junction temperature. The sensitivity (S) of a TC sensor depends on the produced voltage per unit temperature difference (ΔT) which is the Seebeck coefficient (α) differences between the two junction materials ($\alpha_1 - \alpha_2$);[7]

$$S = \alpha_1 - \alpha_2 = (\Delta V_1 - \Delta V_2)/\Delta T = V_{out}/\Delta T \quad (1)$$

However, S for conventional TCs is low because α is low for classical metals. Despite the development of bulk TE materials with high α, they could not be employed for TC sensor applications due to the difficulties in the fabrication of robust long junction wires. Recently, the focus on printed thermoelectrics is growing due to its promising cost-effective manufacturing process of shape-versatile TE devices.[8–13] Consequently, progressions in printed thermoelectrics open up new approaches to fabricating printed TC-based low-cost temperature sensors. Hence, recently a few high-conducting metals and intermetallic alloys have been printed to fabricate TCs and employed as temperature sensors.[14,15] However, the sensitivity lacks behind due to the low α (<50 µV °C^{-1}) of the printed materials.[16,17] High-performance printed TE materials such as Sb/Bi-Te-based alloys offer a pathway to enhancing the sensitivity of the temperature sensor due to their higher

M. M. Mallick, L. Franke, A. G. Rösch, M. Hussein, U. Lemmer
Light Technology Institute
Karlsruhe Institute of Technology
76131 Karlsruhe, Germany
E-mail: mofasser.mallick@kit.edu; uli.lemmer@kit.edu

The ORCID identification number(s) for the author(s) of this article can be found under https://doi.org/10.1002/adfm.202301681

DOI: 10.1002/adfm.202301681

M. M. Mallick
School of Mathematics and Physics
Xiamen University Malaysia
Jalan Sunsuria, Bandar Sunsuria, Sepang, Selangor 43900, Malaysia

M. Hussein
Department of Physics
Faculty of Science
Ain Shams University
Cairo 11566, Egypt

Z. Long, Y. M. Eggeler
Laboratory for Electron Microscopy
Karlsruhe Institute of Technology
76131 Karlsruhe, Germany

U. Lemmer
Institute of Microstructure Technology
Karlsruhe Institute of Technology
76344 Eggenstein-Leopoldshafen, Germany

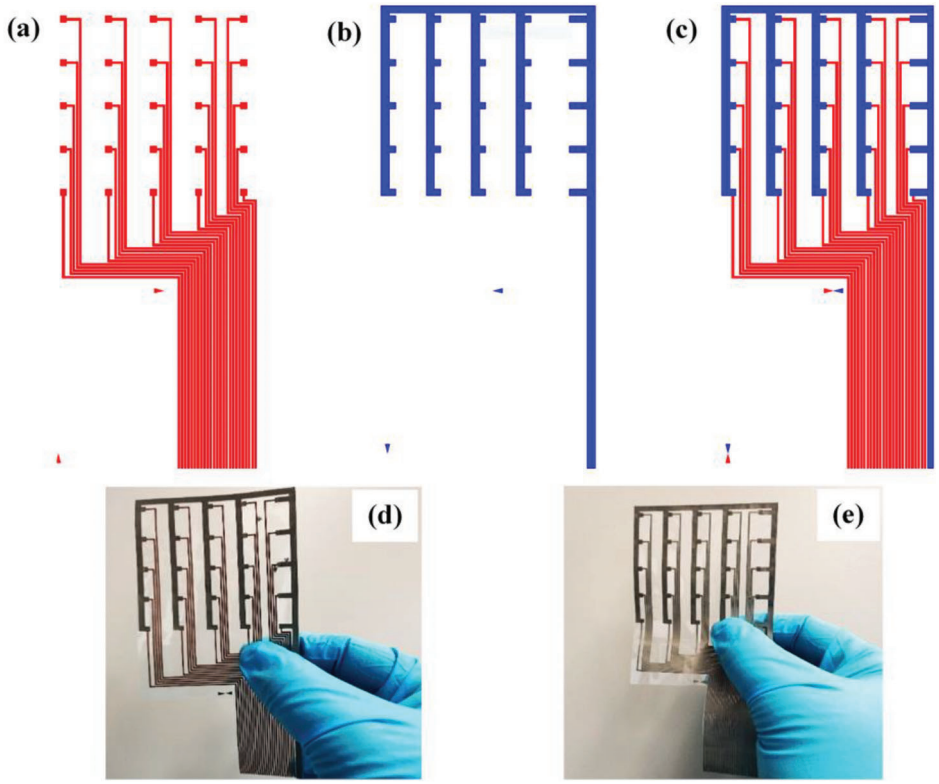

Figure 1. a) The n-type (n-BT) /copper TE leg layout, b) the layout for the p-type (p-BST) leg, and c) the schematic of the temperature sensor array layout. e) The fabricated TSA I and f) TSA II.

α.[18,19] The difficulties in fabricating Sb/Bi-Te-based long cylindrical wire junctions (thermocouples) can be overcome by implementing printing technologies for this class of materials. In addition, temperature array sensors with multiple probing points can be fabricated using printing processes. However, achieving good flexibility and robustness in long Sb/Bi-Te-based printed films with suitable conductivity is a substantial challenge. In our recent work, we have successfully developed a pair of telluride-based high-performance flexible n- and p-type printed TE films via ultra-rapid photonic curing processes.[20,21] This advancement allows us to manufacture low-cost high-performance printed TE films that could be implemented for printed TC-based temperature sensors.

In this work, we demonstrate the fabrication of a pair of high-performance Sb/Bi-Te-based n-type and p-type long flexible printed TE films for sensor applications. First, we synthesize printable inks comprising p-$Bi_{0.5}Sb_{1.5}Te_3$ (p-BST)/n-$Bi_2Te_{2.7}Se_{0.3}$ (n-BT) TE particles and Cu-Se-based inorganic binders. Then, the prepared inks are screen-printed using two different layouts, one for the n-type and another for the p-type leg. We thus fabricate 5×5 temperature sensor arrays (TSA) comprising 25 pixels (c.f. **Figure 1**). The temperature sensor arrays are then dried followed by sintering using a millisecond photonic curing process to form the TC junctions. The temperature sensor arrays are found to be superior in performance with more than two times higher sensitivity compared to the existing thermocouple-based sensors. Furthermore, the disadvantages associated with a conventional thermocouple-based sensor such as low sensitivity, low stability, and low operating temperature range, are overcome. The functionality of the sensor array is demonstrated by integrating it on the surface of a Li-ion battery.

2. Simulation of the TSAs

The finite element method (FEM) via COMSOL Multiphysics 5.6 has been employed to study and analyze the performance of the new design TSA I of a TE generator before the printing process. Specifically, we use the TE module to study heat transfer processes. Through this module, several phenomena, such as heat transfer, conduction, and convection are simulated and analyzed. The temperature at the TC junctions and TC ends are set to 20 and 100 °C, respectively, to provide an 80 °C temperature difference across the whole TSA. To make the simulation more realistic, the properties of TE materials, such as thermal conductivity, Seebeck coefficients, and electrical conductivity, are taken from the experimental data and imported into the COMSOL module. **Figure 2**a shows the simulated temperature variation at the surface for the case of a localized hot spot centered at pixel (3,3). More detailed simulation results are given in the supporting document (c.f. Figure S1, Supporting Information). Due to the temperature gradient, the free electrons on the hot side diffuse and accumulate at the lower temperature surface (cold side), converting the temperature difference into a thermovoltage to electrical power.

The temperature varied from 20 to 100 °C on cold and hot ends. This analysis was carried out in a multislice plot, and the volumetric plot where the mean value is the output voltage of the TSA I (mV). Figure 2b shows the thermovoltage developed at the

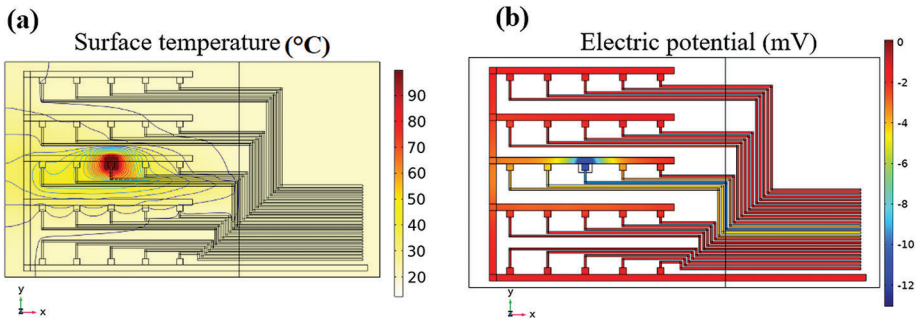

Figure 2. a) Simulation of the temperature distribution around a single pixel (3, 3) source of the TSA I (T_{cold} = 20 °C, T_{hot} = 100 °C). b) The output thermovoltage from the pixel, (3, 3).

above-mentioned pixel. To check the effect of the source size and position on the performance of the reported design. As can be seen from Figure 2, the heat is efficiently transferred and generates voltage.

3. Results

3.1. Microstructural Properties and Mechanical Flexibility Of The Printed TSAs

The high-resolution surface topography of a part of the printed TSA II obtained from a white light interferometer is shown in **Figure 3**a. The overall morphology shows some larger nonuniform regions (see black frame). These surface inhomogeneities appear due to the small deformations of the flexible substrate during flash sintering. However, the magnified image of the printed TCs (red frame) indicates that the surfaces of the TCs are uniform. The pixel legs with 0.7 mm width are separated by a distance of 0.3 mm and they are not overlapping. The SEM images of the p-BST and n-BT printed films indicate two-phase systems comprising the main TE phase and a high-conducting β-Cu_2Se phase (c.f. Figure 3b,c). A detailed analysis of the crystallographic structures and microstructural properties of the two-phase systems including elemental mapping has been discussed in the previous report.[20]

The mechanical robustness of a flexible TSA is vital for different applications on non-flat surfaces. Hence, the mechanical flexibility of the fabricated printed TSAs was studied by record-

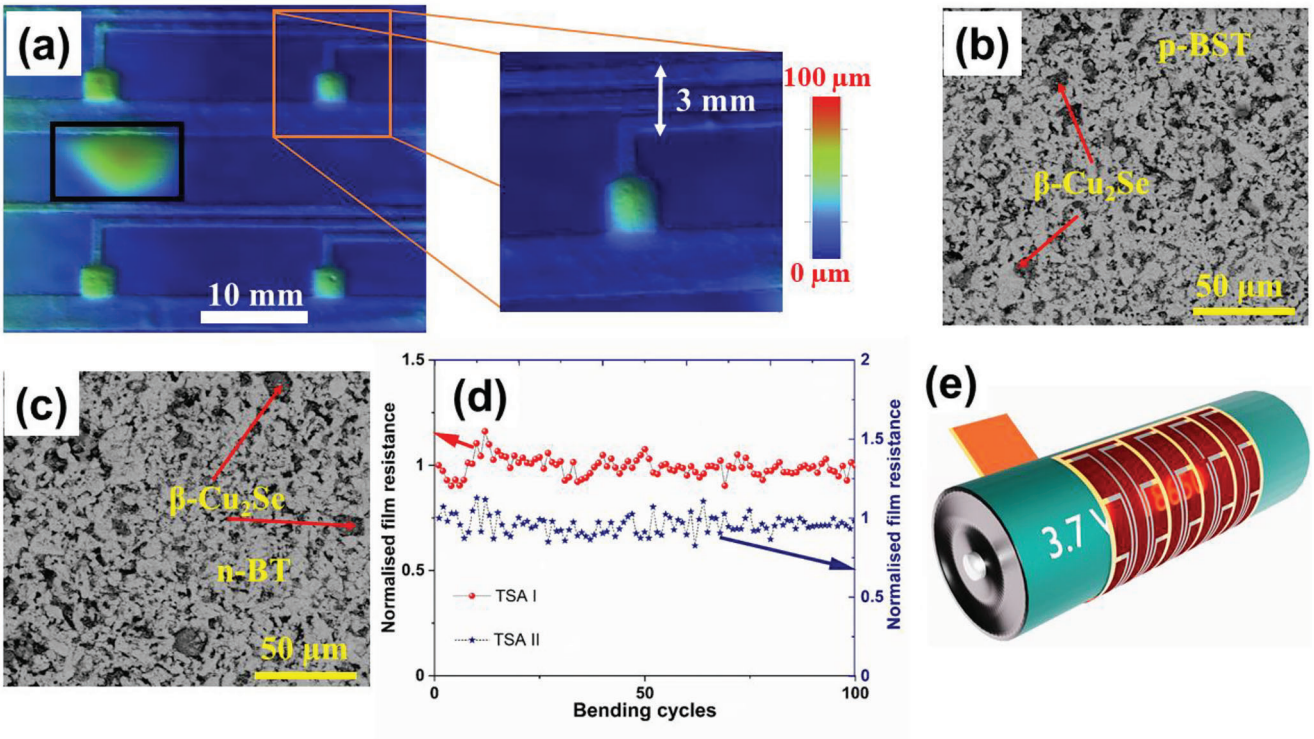

Figure 3. a) The surface topography of the printed TCs obtained from WLI. The SEM microstructures of the printed b) p-BST and c) n-BT films. d) The change in normalized TC resistance of TSA I and TSA II with bending cycles. e) The schematic of the TSA in the bending condition (wrapped around a battery).

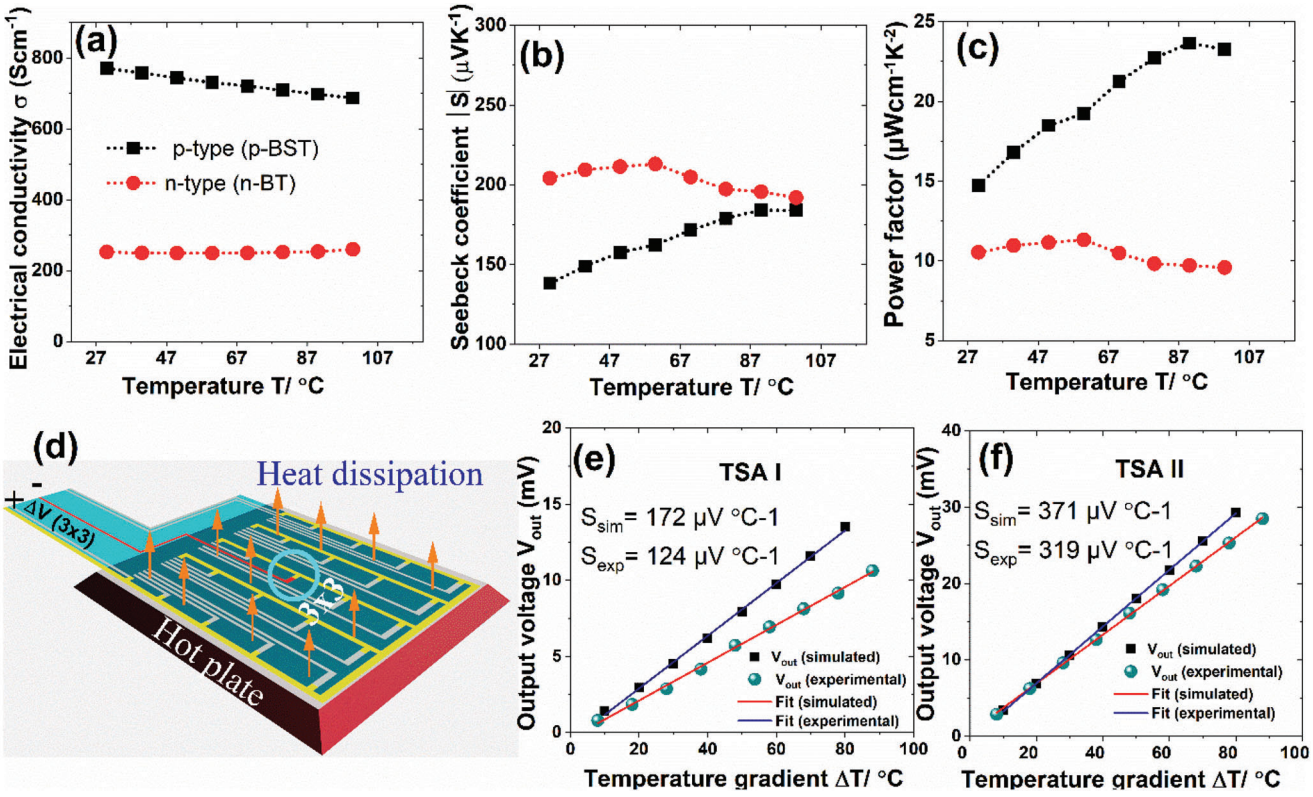

Figure 4. The temperature-dependent thermoelectric parameters a) σ, b) α, and c) power factor ($\alpha^2\sigma$) of the printed p-BST and n-BT films. d) The schematic of the TSA on a hot plate. The experimental and simulated sensitivities (S) of the e) TSA I and f) TSA II estimated from the ΔT dependent voltage output V_{out} corresponding to the pixel (3,3).

ing the TC resistance (R) corresponding to the 3×3 pixel during bending and straightening conditions. The TSAs were bent 100 times in 30 s intervals during the recording of the TC resistance (see Figure 3d). The flexibility test was done by bending the TSAs around a 18 650 Li-ion battery cell with an 18 mm diameter for 100 cycles (see Figure 3e). The change in the R is found to be negligible for both TSAs. The resistances of the (3,3) pixel are found to be within 16% of the initial value for TSA I, and 13% for TSA II, respectively.

3.2. Thermoelectric Performance of the Printed TE Legs and Sensitivities of the TSAs

The sensitivity (S) and responsivity of a thermocouple temperature sensor depend on the TE parameters of the TCs. According to equation 1, the sensitivity S is directly proportional to the resultant Seebeck voltage of the TCs.

On the other hand, the responsivity and detectivity of a thermosensor are inversely proportional to the TC resistance.[22,23] Hence, the printed TCs should exhibit a high power factor to fabricate a highly sensitive temperature sensor. Therefore, the high TE performance n- and p-type printed films in the temperature range from 30 to 100 °C have been employed to fabricate TSAs (c.f. **Figure 4**a–c and Table S1). The electrical conductivity σ is found to be high compared to state-of-the-art printed TE films. The σ for the p-BST film is higher at all temperatures than the n-BT film whereas the Seebeck coefficient α is found to be higher for the n-BT film in the complete temperature range. The resultant power factor ($\alpha^2\sigma$) is calculated to be >10 μW cm^{-1} K^{-2} for both the p- and n-type films. Both results are among the highest report values for printed TE film.[9] Hence, the p-BST and n-BT TE films have been used to fabricate printed TSAs. The detailed thermo-transport phenomena of the printed n-BT and p-BST have been discussed in the previous report.[20]

The average sensitivities (S_{exp}) of the TSAs were estimated from the ΔT dependent output voltage V_{out} corresponding to the middle pixel (3,3) TC junction using Equation 1. The experimental S_{exp} of the TSA I and TSA II has been compared with their simulated S_{exp} (c.f. Figure 4e,f). The variation of the V_{out} with ΔT seems to be linear up to 100 °C. The sensitivities S(T) corresponding to different ΔTs are calculated to determine the temperature in that temperature range more accurately. The average sensitivities (S_{exp}) of the TSA-I and TSA-II are found to be ≈124 and ≈319 μV °C^{-1}, respectively. The sensitivities are more than two times higher than the conventional TCs; copper-constantan and iron-constantan (c.f. Figure S2, Supporting Information). The S_{exp} is found to be lower for TSA-I compared to TSA-II because it comprises only a single tailored TE leg (p-BST) in a thermocouple with copper. The total output voltage $V_{out} = \Delta T(\alpha_1 - \alpha_2)$ is lower in TSA I because of the low Seebeck coefficient of copper. Whereas for the TSA-II both the legs (p-BST and n-BT) in a thermocouple junction possess a high Seebeck coefficient. This enhances sensitivity. It should be noted that the experimental S_{exp}

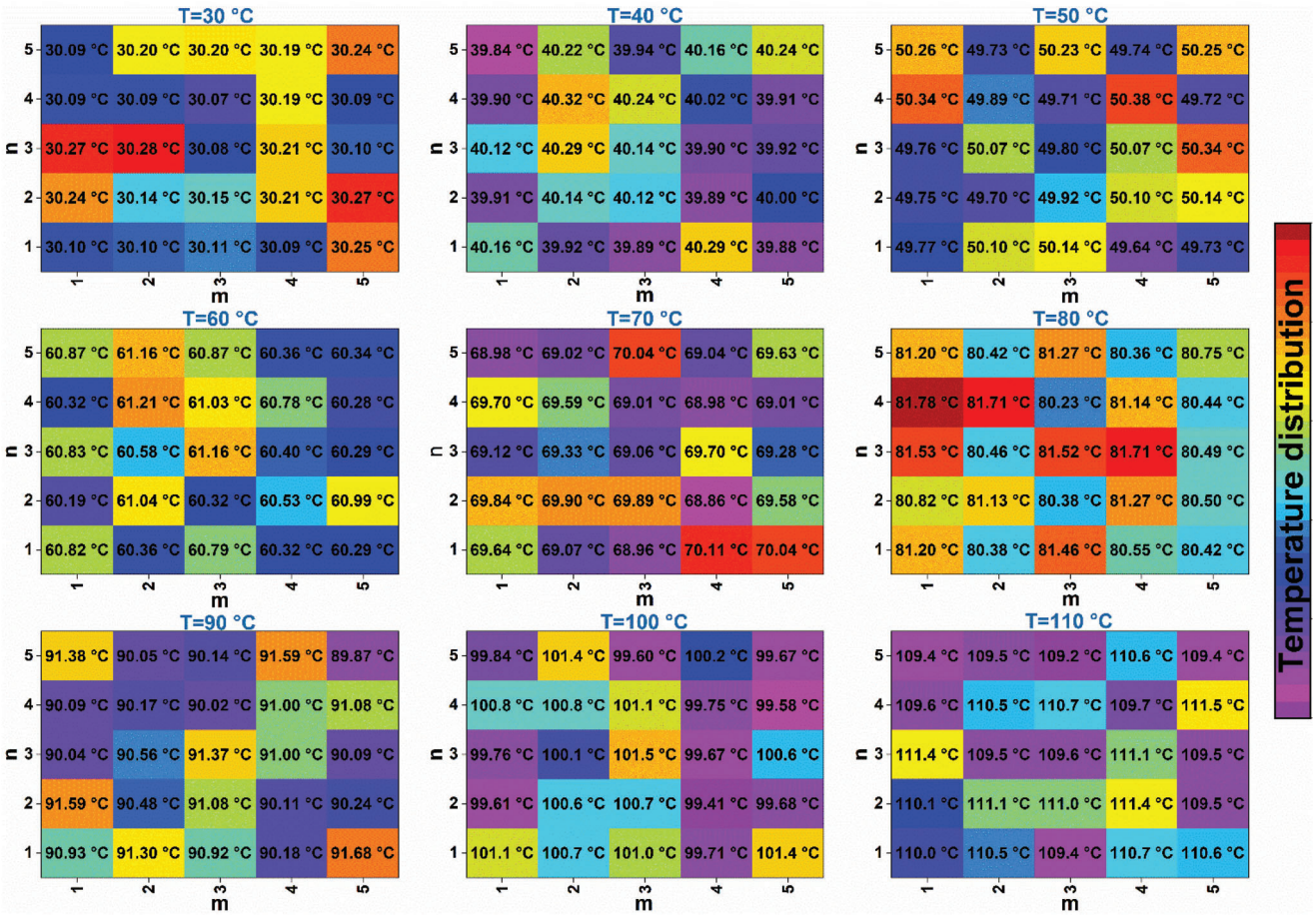

Figure 5. The temperature mapping of a hot surface for different temperatures obtained by 25 pixels of the TSA I.

values for both the TSAs are found to be slightly lower compared to their theoretical values due to the thermal resistance across the insulating substrates and improper thermal contact. The thermal resistance between the heat source and the TSAs lowers the actual ΔT, which leads to a lower thermovoltage. However, the overall S_{exp} values are found to be significantly high compared to the conventional thermocouple-based temperature sensors.

3.3. Performance of the Printed TSA I and TSA II

The performance of the TSAs was studied by detecting unknown temperatures using the determined sensitivities. The TSAs were employed to measure nine different temperatures using the derived sensor parameters. The TSAs were kept on a hot flat surface with nearly homogeneous outward heat flux throughout the surface whereas the other ends of the TSAs were in contact with the ambient air. The temperature of the hot surface varied between 30 and 110 °C during the measurements. The temperatures from 30 °C to 100 °C were determined using corresponding sensitivities of the TSAs and the temperature of 110 °C was estimated using the average sensitivity of the TSAs. The temperature for every 25 individual TCs was determined by changing the hot surface temperature (c.f. **Figures 5** and **6**). It is found that both sensors TSA-I and TSA-II exhibit nearly equal values to the hot plate surface temperatures with only a slight deviation from the actual temperature. The maximum deviation for the minimum actual temperature of 30 °C is ≈0.3 °C for TSA-I and TSA-II. The error increases with increasing hot surface temperature. The maximum errors associated with the temperature of 100 °C are 1.5 and 1.6 °C for TSA-I and TSA-II, respectively. The surface temperatures determined by the TSAs show some non-uniformities. The discrepancy is probably due to local improper thermal contact between the TSAs and the hot surface due to the deformation of the flexible substrates during sintering as seen in Figure 3a. In addition, material defects in the TCs could also alter the voltage output from the individual pixel. This issue could be minimized by improving the thermal contact using a thermal paste.

3.4. Temporal Response of the Printed TSA I and TSA II

The responsitivity studies of the printed TSA I and TSA II have been done by frequently attaching the TSAs on a hot surface and detaching it from the hot surface five times consecutively (c.f. Figure S4, Supporting Information). The hot surface temperatures were maintained at 60 and 80 °C and the output voltages V_{out} corresponding to the pixel (3,3) for both TSAs were recorded

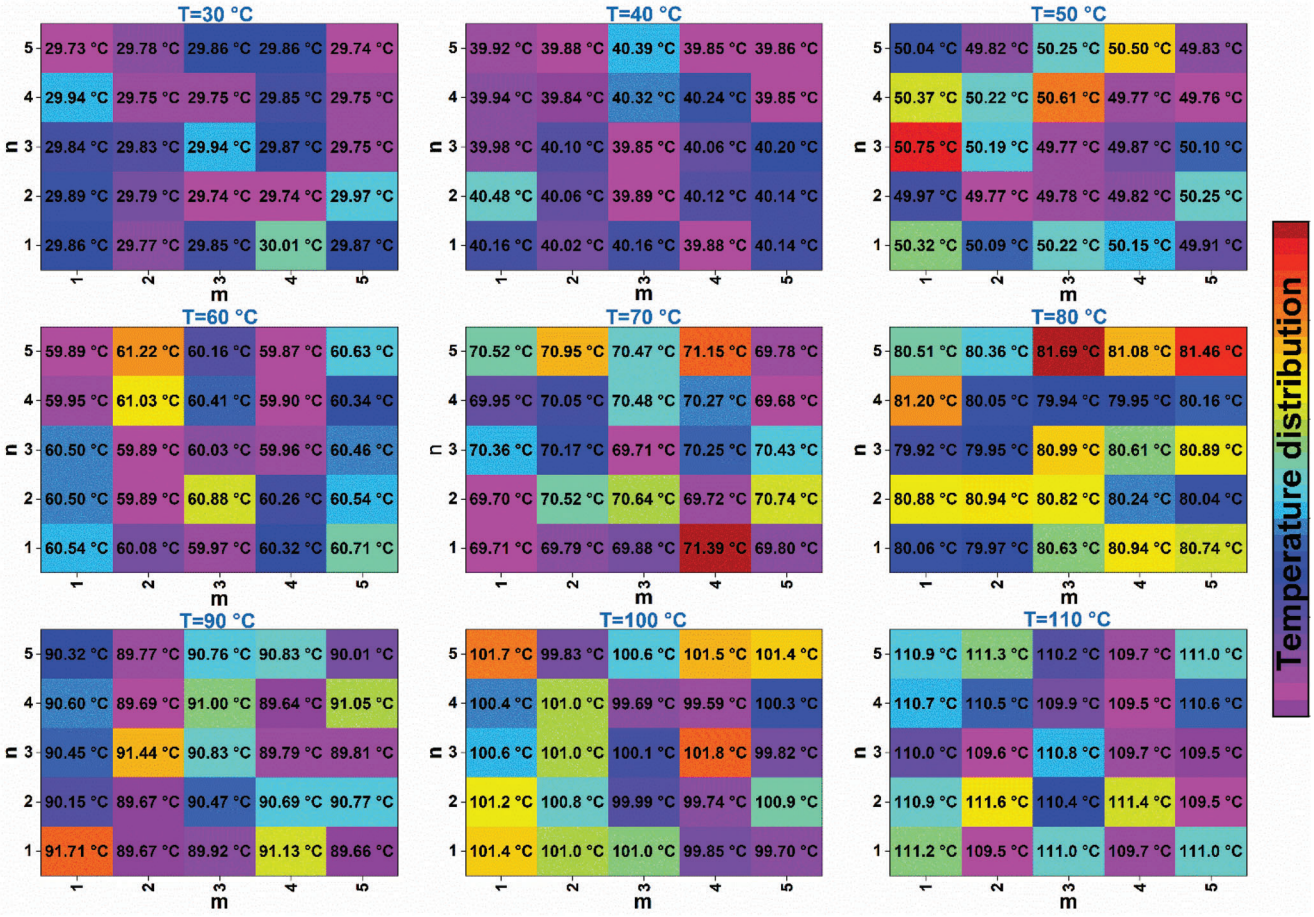

Figure 6. The temperature mapping of a hot surface for different temperatures obtained by 25 pixels of the TSA II.

with time. TSA I and TSA II were brought in contact with the hot surface at five different time delays (t_n = 0, 60, 120, 180, and 240 s) and they were detached from the hot surface after a time delay of the 30 s (t_m = 30, 90, 150, 210, and 270 s). The TSAs were kept in both conditions (attached and detached) for 30 s to reach equilibrium. The responsivity (R_S) of the TSAs is defined as follows;

$$R_S = V_{\text{out}}/V_{\text{max}} \tag{2}$$

where V_{out} is the voltage output corresponding to the pixel (3,3) and $V_{max}(= S \times \Delta T)$ is the maximum reachable voltage according to the sensitivities of the TSAs.

To get an insight into the response curve, the time-dependent rise and fall of the output voltage V_{out} in the first cycle has been modeled for T = 60 °C using the following equation;

$$V_{out} = Ae^{\left(-\frac{t}{\tau}\right)} + B \tag{3}$$

where τ is the time constant, A and B are the fitting parameters. The fit of the time-dependent V_{out} to equation 3 is shown in **Figure 7**. The time constant τ is found to be smaller during the rise than the fall of the temperature. The fitting parameters are given in Table S2 (Supporting Information).

The printed a) TSA II and b) TSA I are demonstrated by wrapping around two different batteries (c.f. Figure S5, Supporting Information). As the temperature of the Li-ion battery rises while discharging, the output voltage of the TSA II increases, as shown in Video S1 (Supporting Information).

4. Discussion

The TSAs not only show flexibility but also yield repeatable output results with a bending cycle (c.f. **Figure 8**a). Our studies on the development of photonically sintered TE films indicate that the pixels with symmetric shape results in better mechanical stability. Ideally, the strain developed during photonic curing is isotropic if the aspect ratio of the film is 1 which makes a rectangular film stable. For lower aspect ratio films, we need to trade off low TC resistance with mechanical stability by controlling sintering power. The pixel output voltage does not depend on the leg dimension; hence, the sensitivity is independent of the pixel leg width. However, the resistance of the pixel leg depends on its width; higher width facilitates lower resistance or a lower signal-to-noise ratio. Hence, lower resistance improves the responsivity of the sensor. Therefore, the pixel legs with higher widths are more stable. However, we were able to fabricate sufficiently robust pixel legs with a width ≥0.3 mm by controlling

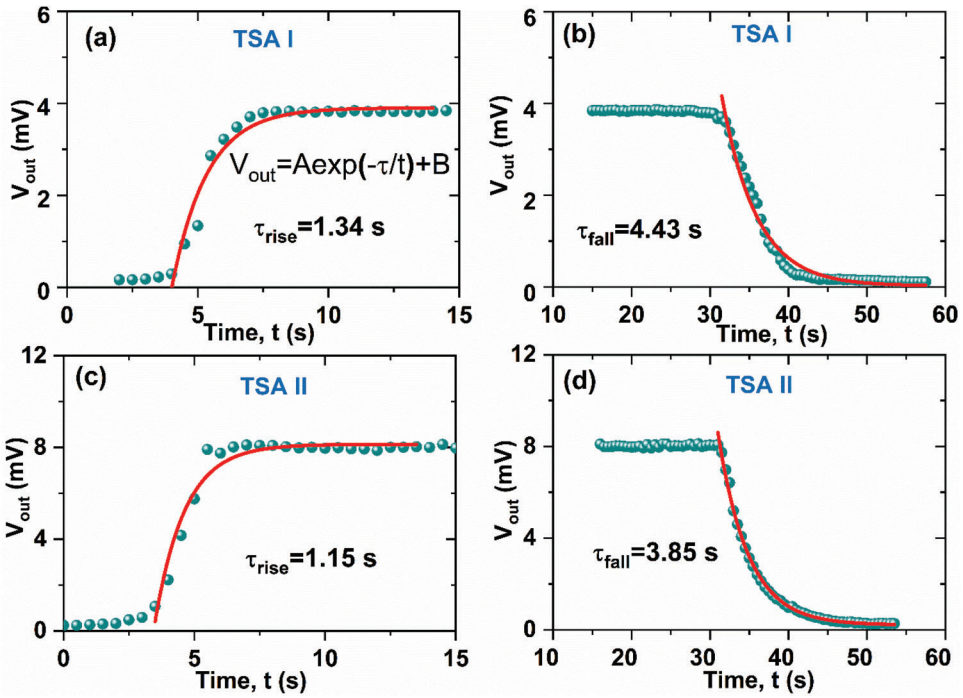

Figure 7. Transient plot of the temperature sensor arrays a,b) TSA I and c,d) TSA II during the rise and fall of the temperature. The time constant τ has been calculated by fitting the curves.

sintering power. No cracks or damages are found in the pixel leg after bending 100 times (c.f. Figure S3, Supporting Information). The TSAs can easily be customized according to the applications and requirements.

The cross-talk effect is one of the major issues for any kind of sensor array that could alter the actual results and it could influence the sensitivity. As the thermovoltage is only generated between hot and cold junctions of thermocouple (n-p) and we only read out the produced voltage of individual directly addressed pixels. During the read-out, only one pixel at a time is connected while all other legs remain disconnected. The TSAs are therefore in principle electrically cross-talk free. The amount of thermal cross talk due to leakage heat current through the pixel legs should also be limited. This is also confirmed by the simulations and experimental results that the thermovoltage from pixel 1 of intact TSA and the same by disconnecting pixel 1 from other pixels are found to be the same (c.f. Figure 8b).

5. Conclusion

In this work, we report a pair of high-performance, flexible, n- and p-type, printed Sb/Bi-Te-based TE films via ultra-rapid photonic curing processes. This approach combines the high Seebeck-coefficients of Sb/Bi-Te alloys with mechanical flexibility and the vast opportunities offered by printing technologies such as large-area processing and direct patterning. The films were used to fabricate [5×5] temperature sensor arrays (TSAs) with more than twice the sensitivity of existing thermocouple-based sensors. The TSAs also had improved linearity, stability, and operating temperature range compared to traditional thermocouples.

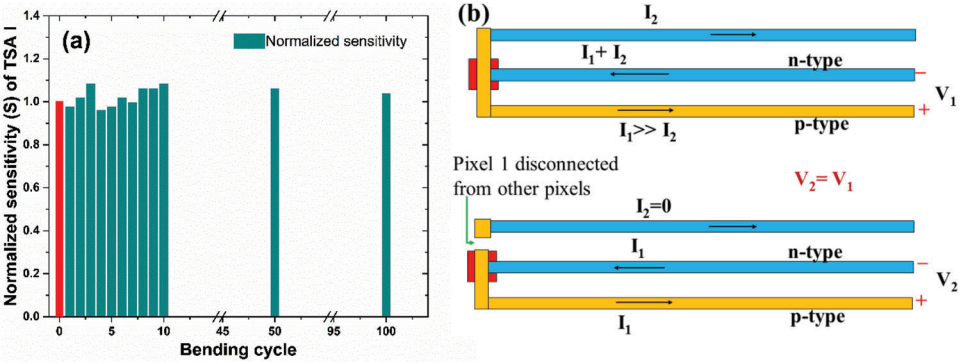

Figure 8. The normalized sensitivity of the TSA I with bending cycles (a). The schematic of the thermovoltage readout of pixel 1 of an intact TSA while it is disconnected from other pixels (b).

The functionality of the TSAs was demonstrated by integrating them on the surface of a lithium-ion battery.

6. Experimental Section

Materials: Ingots of p-type $Bi_{0.5}Sb_{1.5}Te_3$ and n-type $Bi_2Te_{2.7}Se_{0.3}$ (beads, 99.99% trace metals basis, Sigma–Aldrich), Se powder (100 mesh, ≥99.5% trace metals basis, Sigma–Aldrich), Copper powder (spheroidal) (10–25 µm, 98%, Sigma–Aldrich), Polyvinylpyrrolidone (PVP) (average Mw ≈40 000, Sigma–Aldrich), *N*-methyl-2-pyrrolidone (NMP) (anhydrous, 99.5%, Sigma–Aldrich), Silver ink (LOCTITE ECI 1010 E&C), Copper Particle Ink (CP-009, Novacentrix), Polyethylene naphthalate (PEN) (25 µm, DuPont de Nemours), and Kapton (25 µm, DuPont de Nemours).

Preparation of Printable Inks and Fabrication of the Printed TSAs: The n- and p-type TE inks were prepared using p-type $Bi_{0.5}Sb_{1.5}Te_3$ (p-BST) and n-type $Bi_2Te_{2.7}Se_{0.3}$ (n-BT) TE particles by following the previously reported method.[20] The ground p-BST and n-BT TE powders were blended with an inorganic binder (IB) which is comprised of Cu, Se, and PVP in NMP solvent. The final mixtures were ball-milled using a Fritsch Planetary Mill PULVERISETTE 5 premium line at 200 rpm for 45 min. The amount of the Cu-Se metal powder for both p-BST and n-BT was 10 wt.% in the printable ink compositions. The obtained inks were then printed on flexible substrates (PEN and Kapton) by a semi-automated ROKUPRINT screen-printing machine using two different screens (specification of 600 × 300 90-40 y/22° Hitex) with different layouts (c.f. Figure 1). The p-BST ink was printed as the ground line and the copper conductive ink was printed to make 25 junctions to fabricate 5 × 5 TSA (TSA-I). Another 5 × 5 TSA was fabricated using both the p-BST and n-BT inks (TSA-II) by replacing the conducting copper with the n-BT. The printed TSAs were dried at 70 °C for 5–10 min and followed by sintering via the millisecond-photonic-curing process. The detailed sintering methods and parameters have been discussed in the previous report.[20,24]

Characterization Techniques for the Printed Materials and the Sensors: The temperature-dependent electrical conductivity σ and Seebeck coefficient α of the printed n- and p-type TE materials were measured using a Linseis HCS 10. The relative errors associated with the α and σ measurements were 10% and 6%, respectively. The morphology and thickness uniformity of the printed TSAs were studied using a Bruker 3D microscope based on non-contact white-light interferometry (WLI). The microstructural analyses were done using an FEI Quanta 650 environmental scanning electron microscope (SEM). The mechanical flexibility of the TSAs was investigated by recording the change in thermocouple resistance with bending cycles around a roller. The performance of the TSAs was studied using a KEITHLEY Source Measuring Unit 2601B.

Supporting Information

Supporting Information is available from the Wiley Online Library or from the author.

Acknowledgements

The authors wish to acknowledge the Deutsche Forschungsgemeinschaft (DFG, German Research Foundation) under Germany's Excellence Strategy via the Excellence Cluster 3D Matter Made to Order (EXC-2082/1 – 390761711) for financial support. The authors wish to acknowledge funding by the Ministry of Science, Research, and Arts of the state of Baden Württemberg through the MERAGEM graduate school. The German Federal Environmental Foundation (Deutsche Bundesstiftung Umwelt – DBU) through the DBU Ph.D. scholarship program also supported this work. This project received funding from the European Union's Horizon 2020 research and innovation program under Grant Agreement No. 814945-SolBio-Rev.

Open access funding enabled and organized by Projekt DEAL.

Conflict of Interest

The authors declare no conflict of interest.

Data Availability Statement

The data that support the findings of this study are available from the corresponding author upon reasonable request.

Keywords

photonic curing, printed thermocouples, temperature sensor arrays, thermoelectrics

Received: February 13, 2023
Revised: April 4, 2023
Published online:

[1] M. F. Sanad, A. E. Shalan, S. O. Abdellatif, E. S. A. Serea, M. S. Adly, M. A. Ahsan, *Top Curr. Chem.* **2020**, *48*, 378.
[2] O. Farhat, J. Faraj, F. Hachem, C. Castelain, M. Khaled, *Clean. Eng. Technol.* **2022**, *6*, 100387.
[3] D. Zhao, G. Tan, *Appl. Therm. Eng.* **2014**, *66*, 15.
[4] X. L. Shi, J. Zou, Z. G. Chen, *Chem. Rev.* **2020**, *120*, 7399.
[5] A. W. Van Herwaarden, P. M. Sarro, *Sensors and Actuators* **1986**, *10*, 321.
[6] E. Webster, *Metrologia* **2021**, *58*, 025004.
[7] H. S. Lee, *Thermal Design: Heat Sinks, Thermoelectrics, Heat Pipes, Compact Heat Exchangers, and Solar Cells*, John Wiley & Sons, Hoboken, NJ **2010**.
[8] M. Burton, G. Howells, J. Atoyo, M. Carnie, *Adv. Mater.* **2022**, *34*, 2108183.
[9] A. Sarbajna, A. G. Rösch, L. Franke, U. Lemmer, M. M. Mallick, *Adv. Eng. Mater.* **2022**, *25*, 2200980.
[10] M. M. Mallick, A. G. Rösch, L. Franke, A. Gall, S. Ahmad, H. Geßwein, A. Mazilkin, C. Kübel, U. Lemmer, *J. Mater. Chem. A* **2020**, *8*, 16366.
[11] M. M. Mallick, A. Sarbajna, A. G. Rösch, L. Franke, H. Geßwein, Y. M. Eggeler, U. Lemmer, *Appl. Mater. Today* **2021**, *26*, 101269.
[12] A. G. Rösch, A. Gall, S. Aslan, M. Hecht, L. Franke, M. M. Mallick, L. Penth, D. Bahro, D. Friderich, U. Lemmer, *Npj Flex Electron* **2021**, *5*.
[13] A. G. Rösch, L. Franke, M. M. Mallick, U. Lemmer, *Energy Convers. Manag.* **2023**, *279*, 116776.
[14] A. Sheng, S. Khuje, Z. Li, J. Yu, S. Ren, *ACS Appl. Electron. Mater.* **2022**, *4*, 5558.
[15] S. Cruz, G. Azevedo, C. Cano-Raya, N. Manninen, J. C. Viana, *Mater. Sci. Eng. B Solid State Mater. Adv. Technol.* **2021**, *264*, 114929.
[16] Y. Liu, W. Ren, P. Shi, D. Liu, Y. Zhang, M. Liu, Z. G. Ye, W. Jing, B. Tian, Z. Jiang, *Sensors* **2018**, *18*, 958.
[17] H. Li, Y. Yang, J. Liu, *Appl. Phys. Lett.* **2012**, *101*, 073511.
[18] I. T. Witting, T. C. Chasapis, F. Ricci, M. Peters, N. A. Heinz, G. Hautier, G. J. Snyder, *Adv. Electron. Mater.* **2019**, *5*, 1800904.
[19] S. H. Lee, H. Shen, S. Han, *J. Electron. Mater.* **2019**, *48*, 5464.
[20] M. M. Mallick, L. Franke, A. G. Rösch, H. Geßwein, Z. Long, Y. M. Eggeler, U. Lemmer, *Adv. Sci.* **2022**, *9*, 2202411.
[21] M. M. Mallick, L. Franke, A. G. Rösch, S. Ahmad, H. Geßwein, Y. M. Eggeler, M. Rohde, U. Lemmer, *ACS Appl. Mater. Interfaces* **2021**, *13*, 61386.
[22] U. Dillner, E. Kessler, H. G. Meyer, *J. Phys. D. Appl. Phys.* **2011**, *44*, 305102.
[23] X. Guo, X. Lu, P. Jiang, X. Bao, *Adv. Mater.* **2022**, *34*, 2204355.
[24] M. M. Mallick, L. Franke, A. G. Rösch, H. Geßwein, Y. M. Eggeler, U. Lemmer, *ACS Omega* **2022**, *7*, 10695.